FULL PAPER

Solar Cells

ADVANCED
ENERGY
MATERIALS

www.advenergymat.de

How Methylammonium Cations and Chlorine Dopants Heal Defects in Lead Iodide Perovskites

Guangjun Nan, Xu Zhang, Mojtaba Abdi-Jalebi, Zahra Andaji-Garmaroudi, Samuel D. Stranks, Gang Lu,* and David Beljonne*

Lead tri-iodide methylammonium (MAPbI$_3$) perovskite polycrystalline materials show complex optoelectronic behavior, largely because their 3D semiconducting inorganic framework is strongly perturbed by the organic cations and ubiquitous structural or chemical inhomogeneities. Here, a newly developed time-dependent density functional theory-based theoretical formalism is taken advantage of. It treats electron–hole and electron–nuclei interactions on the same footing to assess the many-body excited states of MAPbI$_3$ perovskites in their pristine state and in the presence of point chemical defects. It is shown that lead and iodine vacancies yield deep trap states that can be healed by dynamic effects, namely rotation of the methylammonium cations in response to point charges, or through slight changes in chemical composition, namely by introducing a tiny amount of chlorine dopants in the defective MAPbI$_3$. The theoretical results are supported by photoluminescence experiments on MAPbI$_{3-m}$Cl$_m$ and pave the way toward the design of defect-free perovskite materials with optoelectronic performance approaching the theoretical limits.

1. Introduction

The field of solar energy conversion has witnessed tremendous progress with the development of solar cell devices based on 3D organic–inorganic hybrid perovskites.[1] For the lead tri-iodide methylammonium (MA) perovskites, MAPbI$_3$ (MA ≡ CH$_3$NH$_3^+$), the maximum power conversion efficiency of perovskite solar cells has been raised from 3.8% in the first report[2] to over 20% today.[3] Such an unprecedented improvement has been triggered by the unique features of hybrid perovskites that make them attractive for solar-cell applications, including large optical absorption coefficients and high charge carrier mobility.[1]

Despite these remarkable advances, the mechanism for photoinduced electron–hole (e–h) pair dissociation and transport in lead perovskites is still controversial. Exciton binding energies of 5–16 meV have been reported in MAPbI$_3$,[4] so only a fraction of weakly bound excitons likely coexist with free charge carriers at room temperature under solar illumination conditions.[5] It has been argued that e–h separation could be further assisted by fluctuations in the energy landscape associated with the positional dynamics of MA cations in pristine materials.[6–8] In polycrystalline films prepared from precursor solutions, defects are not as benign as initially thought,[9] as suggested by the recent demonstration of the grain-to-grain variation in photoluminescence (PL) intensity.[10] These reports are seemingly in conflict with the measured, significantly long, charge-carrier diffusion lengths in MAPbI$_3$ films,[11] as these inhomogeneities should act as traps and sources of nonradiative recombination channels.

Very interestingly, the e–h diffusion lengths in iodide-based perovskites can be further enhanced by incorporating a small amount of chlorine anions.[12,13] While it has been claimed that chlorine dopants yield polycrystalline film morphologies with improved charge transport properties,[14,15] possibly by smoothing out structural and energetic discontinuities at grain boundaries[16] or seeding crystallization of higher quality grains,[17,18] recent state-of-the-art studies point to the presence of residual Cl dopants remaining in thin films of MAPbI$_3$.[19,20] The enhanced PL intensity inside the grains with higher Cl concentration[10] may be explained by reduced trap-assisted nonradiative recombination, thereby increasing the lifetime and diffusion length of photoexcited electrons and holes.[14,15,21,22] However, a model relating charge-carrier decay dynamics to atomistic details of the excited-state electronic structure of Cl-doped perovskites is severely lacking.[23]

Here, we address these questions by means of a many-body description of the electronic excitations of pristine and defective perovskites that fully accounts for ground- and excited-state

Dr. G. Nan
MIIT Key Laboratory of Critical Materials Technology
for New Energy Conversion and Storage
School of Chemistry and Chemical Engineering
Harbin Institute of Technology
150001 Harbin, P. R. China
Dr. G. Nan, Dr. D. Beljonne
Laboratory for Chemistry of Novel Materials
University of Mons
Place du Parc 20, B-7000 Mons, Belgium
E-mail: david.beljonne@umons.ac.be
Dr. X. Zhang, Prof. G. Lu
Department of Physics and Astronomy
California State University Northridge
18111 Nordhoff Street, Northridge, CA 91330-8268, USA
E-mail: ganglu@csun.edu
Dr. M. Abdi-Jalebi, Dr. Z. Andaji-Garmaroudi, Dr. S. D. Stranks
Cavendish Laboratory
University of Cambridge
JJ Thomson Ave, Cambridge CB3 0HE, UK

**ADVANCED
SCIENCE NEWS**

www.advancedsciencenews.com

**ADVANCED
ENERGY
MATERIALS**

www.advenergymat.de

structural reorganization, and we provide experimental validation of our theoretical findings by performing photoluminescence experiments on slightly chlorine-doped $MAPbI_{3-m}Cl_m$ ($0 < m < 0.1$) samples. We first show that the spatial extent of the electronic excitations in defective perovskites is controlled by the relative orientation of the MA cations in proximity to the lead and iodine vacancies, irrespective of the crystal phase (similar results are obtained for the cubic and tetragonal phases, so we expect the main conclusions drawn from these calculations to be rather general). We next consider the influence of introducing a small fraction of chlorine ions into defective $MAPbI_3$. Remarkably, our results suggest that the incorporation of a tiny amount of chlorine ions can switch the primary photoexcitations in the defective perovskites from spatially confined to highly delocalized electronic states.

2. Results and Discussion

We start our analysis by noting that single charge carriers can potentially polarize the lattice in ionic perovskites[24,25] and prompt local lattice relaxation, i.e., polaronic effects. Interestingly, the polaronic binding energy can be substantially tuned by MA orientation through induced volumetric strain.[26] Similarly, upon light irradiation, the electronic excitations centered on the inorganic cages might be significantly coupled to the motion of the MA cations, which would result in an energy stabilization following either a direct (electrostatic) or indirect (lattice distortion) mechanism. This can be quantified by the polaronic relaxation energy (E_{pol}), defined as the difference in excitation energies computed from the optimized ground-state and relaxed excited-state geometries.

Local structural rearrangements in the excited states are here assessed in pure- ($MAPbI_3$) and mixed-iodide ($MAPbI_{3-m}Cl_m$) perovskites by using a time-dependent density functional theory (TDDFT) approach recently developed to study electronic excitations in 3D solids.[27] Since we aim at dissecting how defects affect the fate of electron–hole pairs in hybrid perovskites, namely their recombination as probed by photoluminescence experiments, we find it critical to include on the same footing electron–hole and electron–nuclei interactions, as done here. Unless specified, the geometric optimization and charge densities are obtained from Perdew–Burke–Ernzerhof (PBE) functional neglecting spin–orbit coupling (SOC). Yet, we stress that similar results have been obtained on selected control cases using optimally tuned range-separated hybrid DFT functionals[28] and accounting for SOC, thus we believe our results are robust against the level of theory used. We have investigated the influence of MA orientation and of the presence of Cl dopants on the energy and spatial confinement of the lowest electronic excited states in defective perovskites. Native point defects are created by removing Pb^{2+}, I^-, and MA^+ ions from the pristine structures, as these charged vacancies have been demonstrated to be prevalent.[29] Detailed first-principle simulations have indeed reported relatively low and comparable formation energies for these vacancies that translate into defect concentrations up to ≈10^{17}–10^{18} cm^{-3},[9] see below. We note that these concentrations are comparable to the trap densities experimentally reported for nonpassivated polycrystalline films,[30]

and are typically 2–3 orders of magnitude higher than those in high-quality thin films.[10,31,32]

In the absence of defects, the excited-state charge density distribution in both the cubic phase (Figure S1, Supporting Information) and the tetragonal phase (Figure S2, Supporting Information) of $MAPbI_3$ is dictated by the interplay between the organic cations and the inorganic cages[6,7] and largely affected by the dynamic orientation of the MA cations. At any given "instantaneous" configuration (where MA ions are frozen in a local energy minimum on the ground-state potential), one can thus picture hole-rich and electron-rich (or both) spatial regions. Because MA cations have vanishingly small contributions to both the valence band and conduction band edge states,[29,33] the spatial charge distribution for $MAPbI_3$ in the presence of MA vacancy (Figures S3 and S4, Supporting Information) is unaltered with respect to the pristine case (Figures S1 and S2, Supporting Information). The situation is, however, very different for lead and iodine vacancies, as described below. Suppose, first a lead vacancy forms in the vicinity of a hole in one of the instantaneous ground-state configurations above. Because lead vacancies bear two negative charges, they tend to attract hole density (Figure S5, Supporting Information) and repel electron density (Figure S6, Supporting Information). The geometric distortions induced by the reshuffling in electronic density turn the electronic excitation from being delocalized in the optimized ground-state geometry (Figure S5, Supporting Information) to being rather localized in the excited-state geometry (**Figure 1**a). The formation of such a strongly bound e–h pair is supported by the analysis of the hole density of states (DOS), showing both a tail at and discrete levels above the valence band edge (Figure 1b). A small polaron exciton thus forms around the trapped hole with a large polaronic relaxation energy, $E_{pol} = 386$ meV. In contrast, when lead vacancies are located further away from hole-rich regions, delocalized excitations are sustained in both ground-state (Figure S6, Supporting Information) and excited-state geometries (Figure 1c). E_{pol} (= 21 meV) is therefore much smaller and comparable to room temperature thermal energy; concomitantly, no discrete in-gap trap states can be resolved from the DOS (Figure 1d). We stress that a similar picture is obtained whatever the electric polarization state and the crystal phase, i.e., paraelectric (Figure S7–S9, Supporting Information), ferroelectric (Figure S10, Supporting Information), and anti-ferroelectric (Figure S11, Supporting Information) configurations all show the same behavior in hole-rich and hole-poor domains.

The present TDDFT calculations thus strongly support the view that the spatial confinement of the hole and electron wavefunction in the relaxed excited state is highly dependent on the electrostatic environment around defects (here lead vacancies). More specifically, there is a propensity for the dipolar methylammonium groups (with their electron deficient NH_3 termination)[34] to collectively reorient around charged defects, which in turn perturbs the excited-state electronic structure. The deep trap states induced by the presence of lead vacancies in the previous instantaneous snapshots (i.e., in hole-rich regions) are indeed concealed when the MA cations point their NH_3 (instead of CH_3) moiety (Figure S12, Supporting Information) toward the negatively charged defects. Our TDDFT calculations predict this relative orientation (NH_3 in closer contact with
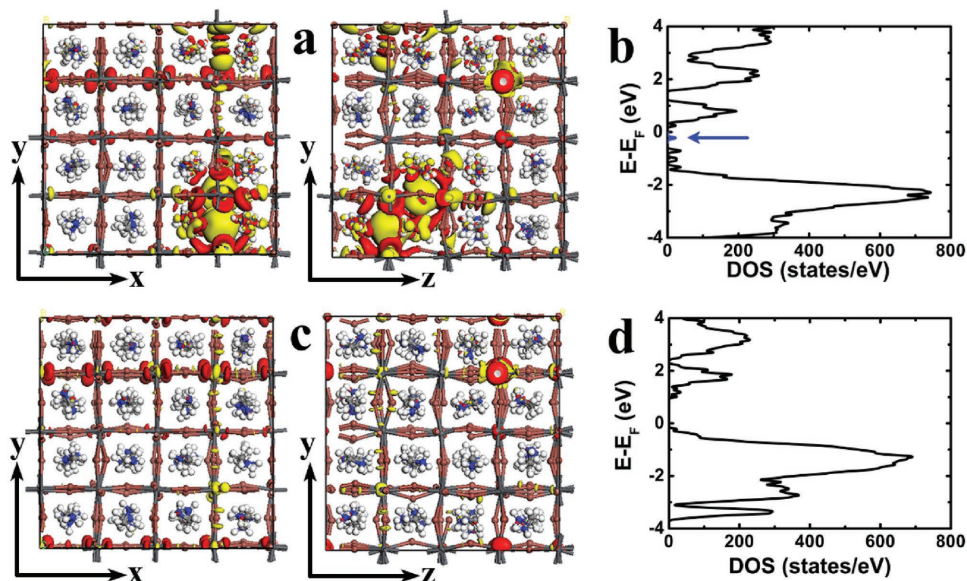
**ADVANCED
SCIENCE NEWS**

www.advancedsciencenews.com

**ADVANCED
ENERGY
MATERIALS**

www.advenergymat.de

Figure 1. Charge densities and DOS in the relaxed geometry of the lowest excited state in MAPbI$_3$ with a single lead vacancy. a) Charge density and b) DOS in defective MAPbI$_3$. The lead vacancy is located at the bottom right of the supercell. The excited-state geometry in (a) is relaxed from the optimized ground-state configuration in Figure S5b (Supporting Information), showing high hole density in vicinity of the lead vacancy. The discrete trap state is highlighted with blue color in (b). c) Charge density and d) DOS in defective MAPbI$_3$. The excited-state geometry in (c) is relaxed from the optimized ground-state configuration in Figure S6b (Supporting Information) with reduced hole density in the vicinity of the lead vacancy. The electron (hole) density is shown in red (yellow) in (a) and (c). The value of isosurface is 1.5×10^{-3} e Å^{-3} in (a) and 1.0×10^{-3} e Å^{-3} in (c).

the vacancy) to be more energetically stable than the reverse situation, in line with simple electrostatic arguments (while, as expected, those in Figure 1a,c with randomly oriented MA cations lies in between). Thus, energetics drives the system toward delocalized electronic excited states by reorienting the MA dipoles in the proximity of lead vacancies. The rotational dynamics of the MA cations (on a picosecond scale)[6] is generally much faster than the nonradiative decay processes (on nanosecond scale),[32,35] hence these structural rearrangements can trigger a release of transiently trapped charge carriers. We speculate that carrier diffusion in the presence of lead defects then proceeds via a sequence of events, involving a dynamic crossover from spatially confined to delocalized states, and vice versa.

This picture is not only valid for lead defects but also prevails in the presence of iodine vacancies. We now pay attention to spatial domains where the orientation of the MA cations translates into high electron density. For the most stable arrangements (Figure S13, Supporting Information) of the iodine vacancies in such electron-rich regions, a self-localization of the electronic excitation ensues upon geometric relaxation (**Figure 2**a) and a discrete trap level emerges below the conduction band edge (Figure 2b). Tracing the geometric deformations in the excited state, we notice that one lead atom close to the iodine vacancy is actually dragged toward that vacancy, leaving behind a broken lead–iodine bond on the opposite side. The resulting localized electronic excitation in Figure 2a is thus prompted by the formation of a lead-centered defect with two excess holes. The accompanying appearance of trap levels close to the conduction band is in fact very reminiscent of the electronic structure of lead interstitials (Figure S14, Supporting Information). Notably, deep states have been identified experimentally as electron

traps.[21,32,36] Since the conduction band is predominantly composed of p orbitals of lead ions, the deep electron traps could possibly originate from the unsaturated lead atoms.[37] Thus, the fingerprints of iodine vacancies and lead interstitials turn out to be very similar and, combined with the results obtained for lead vacancies above, highlight the key role played by lead defects as nonradiative recombination centers. These have been experimentally detected as the main culprit for the degraded performance in perovskite solar cells.[37–39] Interestingly, the photoinduced "brightening" of perovskite PL is associated with a reduction in trap state density through iodine migration.[30] Since iodine interstitials do not break Pb—I bonds and contribute to inefficient traps (Figures S15 and S16, Supporting Information), we propose that lead defects are healed, at least partly, by iodine anions moving to lead defects and repairing the lead–iodine bonds, thereby restoring extended electron wavefunctions. Here also, proper orientation of the MA cations can shift the electron distribution away from the iodine vacancies, so that no trap levels appear in the band gap irrespective of the electric polarization (Figure 2c,d and Figures S17–S19 (Supporting Information)) and crystal phase (Figure S20, Supporting Information). The TDDFT calculations predict the MA cations pointing their electron-rich CH$_3$ moiety toward the positively charged defects to be more energetically stable, so here again, thermodynamics favors a shift of the electron distribution away from the iodine vacancies and delocalized electronic excitations. We notice that depending on the orientation of the MA cations, iodine vacancies yield a distribution of electron traps going from deep levels ($\approx$0.6–1.1 eV below the conduction band) to shallow levels (<0.1 eV) (Figure S21 and Table S1, Supporting Information). The presence of such traps is consistent with the subgap density of states distributions
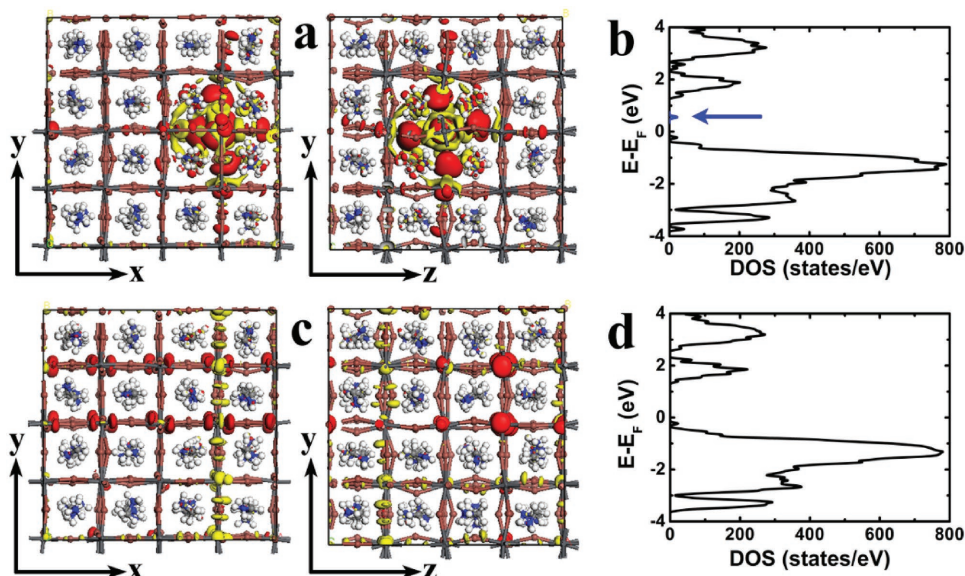
**ADVANCED
SCIENCE NEWS**

www.advancedsciencenews.com

**ADVANCED
ENERGY
MATERIALS**

www.advenergymat.de

Figure 2. Charge densities and DOS in the relaxed geometry of the lowest excited state in MAPbI$_3$ with a single iodine vacancy. a) Charge density and b) DOS in defective MAPbI$_3$. The iodine vacancy is located at the middle right of the supercell. The excited-state geometry in (a) is obtained by relaxing the optimized ground-state configuration in Figure S13b (Supporting Information), where two lead ions are sitting on both sides of the iodine vacancy in a high electron density region. The discrete trap state is highlighted with blue color in (b). c) Charge density and d) DOS in defective MAPbI$_3$. The excited-state geometry in (c) is obtained by relaxing the optimized ground-state configuration in Figure S17b (Supporting Information), where two lead ions are sitting on both sides of the iodine vacancy in a low electron density region. The electron (hole) density is shown in red (yellow) in (a) and (c). The value of isosurface is 1.5×10^{-3} e Å^{-3} in (a) and 1.0×10^{-3} e Å^{-3} in (c).

reported experimentally,[40,41] and is expected to have a substantial impact on recombination of charge carriers.[32,42]

We stress that these results: (i) are robust against the level of theory used, namely a similar picture is obtained by including SOC effects (Figure S22, Supporting Information) or by using optimally tuned range-separated hybrid DFT functionals (Figure S23, Supporting Information); and (ii) are not inconsistent with hybrid functional plus SOC ground-state electronic structure calculations.[43] In fact, both the set of calculations when performed at the ground-state geometry indicate iodine vacancies to be shallow traps (Figures S17–S20, Supporting Information). The deep in-gap trap states in Figure 2c,d develop only once lattice relaxation processes in the excited state (exciton–polaron effects) are switched on, a phenomenon that has been overlooked in previous DFT studies.[9,19,43] For iodine interstitials, both the present PBE (Figure S15, Supporting Information) and the hybrid relativistic DFT calculations with SOC at the ground-state configurations[43] yield an energy level above the valence band edge, yet at slightly different energies (0.22 vs 0.15 eV). However, the corresponding charge densities (Figure S15, Supporting Information) show some degree of (de)localization along different spatial directions, both in the ground-state and excited-state geometries. Overall, we thus expect iodine interstitials to be rather inefficient traps in comparison to iodine vacancies.

MAPbI$_3$ perovskite films are not as spatially homogeneous as originally thought.[44,45] Besides the phenomenon of light-induced halide migration discussed above, films synthesized from Cl-containing precursors typically contain a tiny amount of residual chlorine dopants ($m < 0.12$ in MAPbI$_{3-m}$Cl$_m$).[13,19,20] Although it is difficult to distinguish between the effects of the chloride ions on nucleation of high quality grains from the

impact of residual chloride in the final films,[46] there is now strong collective evidence that residual chloride dopants have a positive effect on the optoelectronic properties.[10,12–20,47–49] Cl-doped MAPbI$_3$ films consistently have a lower trap density than their Cl-free counterparts by 1–2 orders of magnitude.[15,49,50] Recent microscale measurements revealed a positive correlation between local Cl concentration and local PL intensity,[10] suggesting that nonradiative processes, associated with defect densities, are hindered by Cl incorporation not only in between, but also inside the grains.

To understand the role of chlorides on the enhanced PL intensity, we considered configurations where iodine ions are progressively replaced by chlorides, corresponding to MAPbI$_{3-m}$Cl$_m$ with m ranging from 0.015 to 0.06. Compared to pristine bulk sites, this substitution is predicted to be energetically favored on sites close to vacancies because these provide a larger freedom to accommodate the stronger (and shorter) Pb–Cl bonds, in line with the location of Cl ions in perovskite films.[16] Remarkably, our calculations show that the local geometric distortions taking place in the lowest excited states of Cl-free defective MAPbI$_3$ (especially for those ions in the proximity of lead vacancies, **Figure 3**a,b) are suppressed even at moderate Cl ion concentrations ($m \approx 0.3$), see Figure 3c. As a consequence, we observe a localized-to-delocalized transition (from Figure 1a to Figure 3d) of the excited-state charge densities together with a substantial decrease in E_{pol}. Correspondingly, the discrete level expelled from the valence band edge (Figure 3e) in the pure-iodide case now merges into the valence band as Cl anions are substituted for iodides (Figure 3f). This is accompanied by a shift of the Fermi level away from the conduction band, in line with the experimental observation.[51]
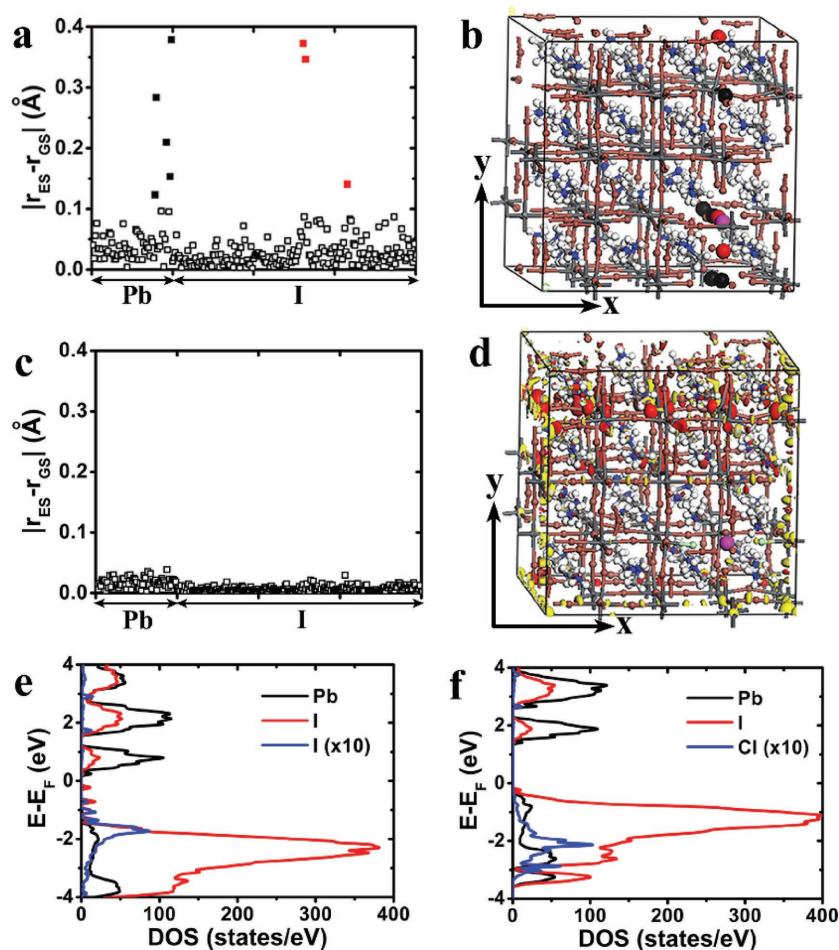
Figure 3. Effects of Cl doping in MAPbI$_3$ with a single lead vacancy. a) Atomic displacements in MAPbI$_3$ from the optimized ground-state geometry in Figure S5b (Supporting Information) to the relaxed excited-state geometry in Figure 1a. b) The ions with the largest displacements. Pb^{2+} (solid black) and I$^-$ (solid red) in (a) are shown with the same color code. c) Atomic displacements in MAPbI$_{3-m}$Cl$_m$ from the optimized ground-state geometry to the relaxed excited-state geometry in (d); the location of two chlorine ions (green color) is indicated. d) Charge densities in the relaxed geometry of the lowest excited state for MAPbI$_{3-m}$Cl$_m$. The electron (hole) density is shown in red (yellow). The value of isosurface is 1.0×10^{-3} e Å^{-3}. The removed Pb^{2+} ion (magenta color) in (b) and (d) is shown as a guide to the eye for the position of Pb vacancy. e) pDOS for the relaxed excited-state geometry in Figure 1a. f) pDOS for the relaxed excited-state geometry in (d). The pDOS of the two substituted iodine ions (blue line in (e)) in MAPbI$_3$ and for the replacing chlorine ions (blue line in (f)) in MAPbI$_{3-m}$Cl$_m$ are zoomed tenfold.

Our rationale for these findings is as follows. Chlorine has much larger electronegativity and ionization potential than iodine, hence substitution of iodides by chlorides should lead to the appearance of Cl-rich occupied levels lying deeper in the valence band. This is confirmed by the analysis of the partial DOS (pDOS), see Figure 3e,f (and holds true whether SOC effects are included or not, see Figure S24 in the Supporting Information). Thus, the mobile holes at the valence band top tend to spread out away from the chlorides and thus also from their preferred spatial confinement around lead vacancies, hence "avoiding" the defects. The vacancies could still act as scattering centers, reducing the charge carrier mobility but not clamping the holes any longer, in essence healing the material from a charge transport perspective.

Cl dopants also suppress the formation of discrete traps associated with iodine vacancies. Recall that in the case of the labile lead–iodine bonds, electron trap levels develop inside the gap because of the weakening/breaking of a Pb—I bond close to the vacancy, with the iodine vacancy ultimately behaving similar to a lead interstitial. As lead binds more strongly to chlorine (than to iodine), this is alleviated in the case where iodides are substituted with chlorides in the geometric arrangement shown in **Figure 4**b. The pDOS in Figure 4a shows that the lead atoms responsible for the emergence of electron traps in Cl-free perovskites now contribute to crystal orbitals well inside the conduction bands. As a result, instead of being spatially confined in the pure-iodine case (Figure 2a), the lowest electronic excitations are delocalized away from the vacancies in Cl-doped MAPbI$_3$ (Figure 4c). The present TDDFT calculations thus suggest that the reduced (trap-assisted) nonradiative recombination of the e–h pairs[10] and the resulting improved charge carrier lifetime[12,15,22] and diffusion length[12] in Cl-doped perovskites stem at least in part (in addition to the improved morphology) from the extended delocalized states sustained by the mixed perovskites in presence of even tiny amounts of chlorine ions.

To validate our theoretical findings, we experimentally prepared thin films of MAPbI$_{3-m}$Cl$_m$ with the Cl content in the precursor films ranging from $m = 0$ to $m = 0.1$ (see the Experimental Section for sample preparation details). The film properties such as absorption (Figure S25, Supporting Information) and morphology (Figure S26, Supporting Information) do not dramatically change with chloride addition, allowing us to mostly isolate the impact of chloride on the charge carrier recombination properties in the series. Photoluminescence is an effective probe for traps, which impact the PL properties by introducing nonradiative decay pathways for charge carriers.[52] In **Figure 5**a, we show that the PL intensity and the measured photoluminescence quantum efficiency (PLQE) increases with addition of Cl. We note that the internal PLQE values will be much higher ($\approx$10–15%)[50] owing to light collection losses in the external measurement due to poor light out-coupling and photon recycling effects that depend on the thin film geometry.[31,53] The PLQE increases from 1.3% ($m = 0$) to 2.3% ($m = 0.05$) before dropping again to 2.1% for higher Cl content ($m = 0.1$). This trend is also reflected in the corresponding time-resolved PL decays (Figure 5b), where recombination is slowed down as we increase the Cl content to a maximum of $m = 0.05$, before decreasing again for $m = 0.1$. We have recently developed a model that is able to describe the
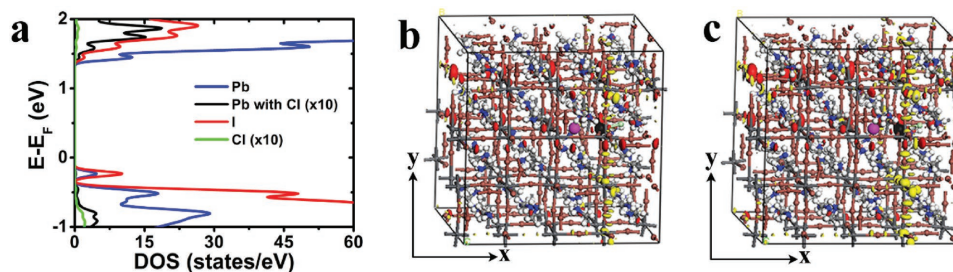
**ADVANCED
SCIENCE NEWS**

www.advancedsciencenews.com

**ADVANCED
ENERGY
MATERIALS**

www.advenergymat.de

Figure 4. pDOS and charge densities of the lowest excited state for $MAPbI_{3-m}Cl_m$ in presence of a single iodine vacancy. a) pDOS for the geometry in (b). The black and green lines pDOS correspond to the bound lead ion (shown by a black color in (b)) and chloride, respectively. The blue line pDOS shows the contributions from all other lead ions. The pDOS indicated by the black and green lines is zoomed tenfold. b,c) Charge densities of the optimized ground-state geometry and relaxed excited-state geometry for $MAPbI_{3-m}Cl_m$, respectively. One iodine ion of the defective $MAPbI_3$ in Figure S13b (Supporting Information) is substituted with one chlorine ion (indicated by the green color) close to the iodine vacancy. The removed I^- ion (magenta color in (b) and (c)) is shown as a guide to the eye for the position of the iodine vacancy. The electron (hole) density is shown in red (yellow) with the isosurface value being 1.0×10^{-3} e $Å^{-3}$ in (b) and (c).

PL kinetics in perovskite films in the presence of N_T electron subgap trap states,[30,42] and we use this model to fit the data to quantify the changes (gray lines in Figure 5b). We find that the trap density decreases by almost an order of magnitude with Cl addition, from 4.7×10^{16} cm^{-3} ($m = 0$) to 7×10^{15} cm^{-3} ($m = 0.05$) (Figure 5b inset; see the Experimental Section and Figure S27 in the Supporting Information for low fluence results). These experimental data are consistent with the theoretical results above.

The formation energies for point defects in $MAPbI_3$ have been calculated by Yin et al.:[9] These vary from 0.29 to 2.68 eV for lead vacancies, from 0.67 to 1.87 eV for iodine vacancies, and from 0.23 to 1.42 eV for iodine interstitials. Using a Boltzmann distribution, these formation energies turn into upper limits at room temperature for defect concentrations in single crystals of $\approx 3.6 \times 10^{16}$ cm^{-3} for lead vacancies, $\approx 2.7 \times 10^{10}$ cm^{-3} for iodine vacancies, and $\approx 1.2 \times 10^{18}$ cm^{-3} for iodine interstitials. We should stress, however, that these numbers should be considered with caution as: (i) small errors in formation energies have a dramatic influence on concentrations; and (ii) most importantly, these data refer to single crystals while higher defect concentrations are expected in polycrystalline films

because of grain boundaries and deviation from stoichiometry at grain surfaces, etc. By fitting photoluminescence kinetics data in presence of electronic subgap trap states[30] (Figure 5b), we estimate trap concentrations of 10^{15}–10^{16} cm^{-3}, in line with previous investigations.[54,55] From a comparison with the predicted defect concentrations, one would tentatively conclude that the traps arise mainly from the most numerous lead vacancies and iodine interstitials. The reality is a bit more complex, however, as iodine defects are characterized by low transport activation barriers[56] and are thus very mobile. In the close to stoichiometric (at the macroscopic scale) films of deQuillettes et al.,[30] the presence of interstitial iodides is therefore necessarily accompanied with iodide vacancies, hence it is difficult to disentangle the relative contributions from the various types of defects.

3. Conclusions

In conclusions, our work points to two key findings that highlight the importance of electron–phonon couplings in perovskites and the extraordinary sensitivity of these interactions to
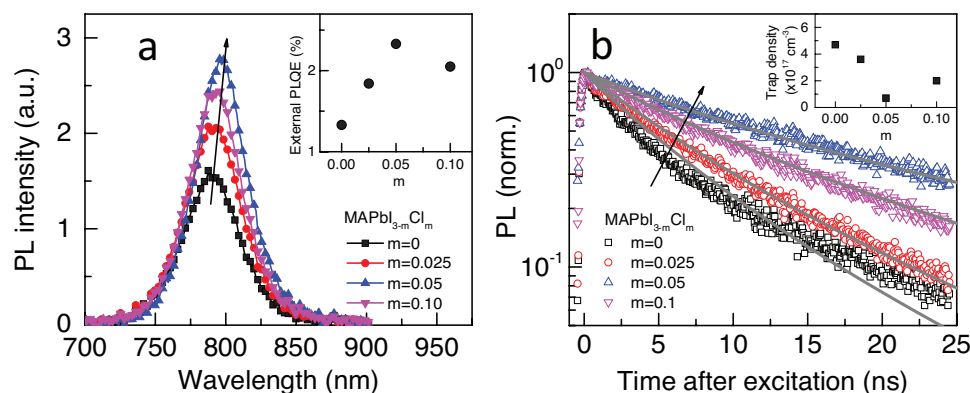

Figure 5. Photoluminescence (PL) properties of $MAPbI_{3-m}Cl_m$ films controllably doped with small amounts of Cl in the precursor solutions. a) PL intensity from $MAPbI_{3-m}Cl_m$ thin films with increasing chloride content (m) illuminated with a 532 nm CW laser. Inset: External PLQE of the films averaged across three measurements on each sample (relative error <10% for each). b) Time-resolved PL measurements of the series zoomed in over the key window. The films were photoexcited with a 407 nm pulsed laser with a fluence of 3.2 μJ cm^{-2} $pulse^{-1}$. The solid gray lines are fits to the data using a trap model[41] with the resulting trap densities shown in the inset.
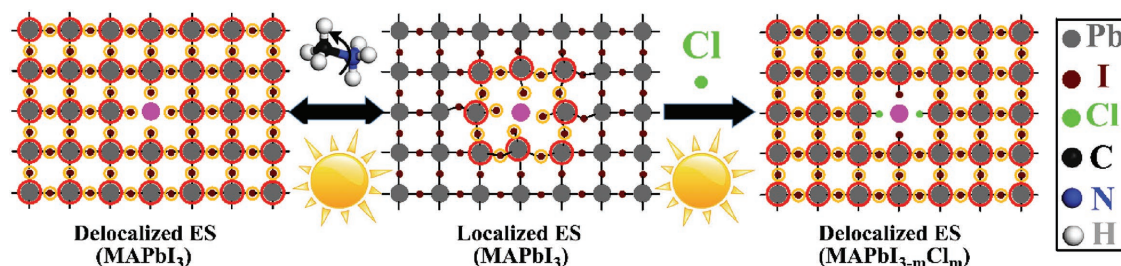
Figure 6. Schematic picture of the dynamic (MA orientation) and static (Cl doping) healing mechanisms. The crossover from spatially localized to delocalized excited states (ES) in defective perovskites is reflected by the extension of charge densities in the vicinity of the vacancies (shown in magenta color). The electron (hole) density is shown by red (yellow) circles on lead (iodine) ions.

the charge distribution in the proximity of defects. Specifically, we have demonstrated that the orientation of MA cations settles the local excited-state charge distribution in the vicinity of defects. The local geometric distortions in the excited state and the associated trap states for both lead and iodine vacancies in defective MAPbI$_3$ can be dynamically healed as MA cations rotate toward their thermodynamic configuration. This is confirmed by a substantial decrease in E_{pol} and a reduced deformation of the inorganic lattice in the vicinity of the chemical defects. This peculiar capability of escaping traps in defective MAPbI$_3$ perovskites leads to the long charge carrier lifetimes and diffusion lengths. We speculate that the charge carrier diffusion in MAPbI$_3$ films occurs by a repeated sequence of localized-to-delocalized crossovers, which also affect nonradiative recombination. Remarkably, a transition from defect-localized to spatially extended electronic excited states is predicted from our calculations for Cl-doped defective perovskites. The localized excited state in defective MAPbI$_3$ can thus be healed when a small amount of Cl ions replace iodides in the defective MAPbI$_3$ perovskites. The stronger electronegativity of chlorine (vs iodine) and the associated more rigid bonds these form with lead ions result in suppressed lattice distortions and shift the density of holes and electrons far from the defect centers. Overall, we attribute the observed healing defects to dynamic reorientation of the methylammonium cations and local lattice distortions around chlorine dopants in vicinity of the vacancies, as sketched in **Figure 6**. We thus expect these healing effects to be suppressed in pure inorganic lead-halide perovskites (like, e.g., CsPbI$_3$), which might be the reason for their lower photoconversion quantum yields.[57] Finally, on a modeling perspective, the present work suggests that treating electron–hole and electron–nuclei interactions on the same footing is critical to reveal the formation of trap states in defective MAPbI$_3$ under solar illumination, which might be important toward exploring the environment effects on the photophysics of organic–inorganic halide perovskites.[58,59]

4. Experimental Section

Computational Details: The cubic and tetragonal phases of MAPbI$_3$ were modeled. The geometry optimization of the primitive cell was carried out by using density functional theory (DFT) with a plane-wave basis set, as implemented in the Vienna ab initio simulation package.[60] The semiempirical DFT-D$_2$ method was used to account for the van der Waals corrections.[61] Energy convergence criterion was set to be 10^{-5} eV

and atomic positions were relaxed until the forces on each atom along each direction were smaller than 0.02 eV Å^{-1}. A k-mesh of $7 \times 7 \times 7$ was used during the geometry relaxation. The optimized primitive cell was then periodically expanded, generating a $4 \times 4 \times 4$ supercell with 768 ions for the cubic phase and a $2 \times 2 \times 2$ supercell with 384 ions for the tetragonal phase. Point vacancies were created by removing Pb^{2+} ion, I$^-$ ion and MA$^+$ cation, respectively, from the supercell with the fixed lattice constants. Based on the projected augmented wave pseudopotentials[62] and the PBE functional[63] and using a cutoff energy of 400 eV, the ground-state calculations were then performed at the Γ point, an approach that has been shown to reasonably predict the band gap and defect properties for the studied systems.[64,65] The energy convergence criterion was set to be 10^{-4} eV and the atomic positions were relaxed until the forces on each atom along each direction were smaller than 0.04 eV Å^{-1}. Based on the DFT fully optimized ground-state supercells (with and without defects), a recently developed TDDFT scheme was applied to assess geometry relaxation in the excited state.[27] This TDDFT method targets large-scale systems in the framework of linear response theory and is implemented in conjunction with the use of pseudopotentials and plane-wave basis set. The ionic forces and charge densities in the excited states are obtained by the derivatives of the Lagrangian functional with respect to ionic position and external potential, respectively. The PBE results presented in the paper are consistent with those obtained using an optimally tuned range-separated hybrid functional[28] TDDFT approach for large-scale systems.[66] More details for the TDDFT formalism can be found in the Supporting Information. Notably, to get converged charge densities in the lowest-energy excited states, all of the unoccupied orbitals have to be included in TDDFT calculations, whereas only a few tens of occupied orbitals are sufficient due to the low DOS at the valence band maximum.[33] As a result, the lower-lying occupied orbitals from Cl contents play a negligible role in determining the charge densities of the lowest-energy excited states (Figure S28, Supporting Information).

Perovskite Film Fabrication: The organic cations were purchased from Dysol; the lead compounds from TCI; dimethylformamide (DMF) from Sigma-Aldrich. The perovskite (MAPbI$_{3-m}$Cl$_m$) precursor solutions were prepared by dissolving 1.2 M methylammonium iodide and 1.2 M PbI$_2$ for pristine ($m = 0$), 1.185 M PbI$_2$ and 0.015 M PbCl$_2$ ($m = 0.025$), 1.170 M PbI$_2$ and 0.030 M PbCl$_2$ ($m = 0.050$), and 1.140 M PbI$_2$ and 0.06 M PbCl$_2$ ($m = 0.100$) in anhydrous DMF. The perovskite solutions were then spin coated in a two-step program at 1000 and 6000 rpm for 10 and 30 s, respectively. During the second step, 50 µL of chlorobenzene was dripped on the spinning substrate 10 s prior to the end. All the perovskite films were annealed at 100 °C for 30 min.

Optical Characterization and Trap Model: The steady-state optical properties of perovskite films were studied using UV–visible absorption and PL spectroscopy. The absorption spectra of perovskite films were recorded with a UV–Vis–NIR spectrophotometer (CARY-5) in transmission mode. Fluorescence spectra and fluorescence decay kinetics were recorded on a spectrofluorometer Fluorolog 322. Fluorescence spectra were recorded by exciting the samples with 407 nm continuous-wave (CW) laser and scanning the emission monochromator

from 500 to 850 nm. The same spectrometer working in a single-photon counting mode was used for the measurements of PL decay kinetics. Picosecond pulsed diode laser head NanoLED-405LH (Horiba) emitting <200 ps duration pulses at 407 nm with repetition rate of 40 MHz and fluence of 3.2 μJ cm^{-2} pulse^{-1} was used as an excitation source. The PL kinetic data were fit using the recent trap model, which is described in detail by Stranks et al.[42] and deQuilettes et al.[30] The following parameters were set to be the same as the previous work: $R_{pop} = 2 \times 10^{-10}$ cm^3 s^{-1}, $R_{dep} = 8 \times 10^{-12}$ cm^3 s^{-1}, and fix $\gamma_0 = 5 \times 10^7$ s^{-1}, leaving the only fitting parameter to be the trap density N_T.

PLQE Measurements: Perovskite films were placed in an integrating sphere and were photoexcited using a 532 nm continuous-wave laser. The laser and the emission signals were measured and quantified using a calibrated Andor iDus DU490A InGaAs detector for the determination of PL quantum efficiency. The external PLQE was calculated from measurements by de Mello et al.[67]

Supporting Information

Supporting Information is available from the Wiley Online Library or from the author.

Conflict of Interest

The authors declare no conflict of interest.

[1] J. S. Manser, J. A. Christians, P. V. Kamat, *Chem. Rev.* **2016**, *116*, 12956.

[2] A. Kojima, K. Teshima, Y. Shirai, T. Miyasaka, *J. Am. Chem. Soc.* **2009**, *131*, 6050.

[3] D. A. Egger, A. M. Rappe, L. Kronik, *Acc. Chem. Res.* **2016**, *49*, 573.

[4] A. Miyata, A. Mitioglu, P. Plochocka, O. Portugall, J. T.-W. Wang, S. D. Stranks, H. J. Snaith, R. J. Nicholas, *Nat. Phys.* **2015**, *11*, 582.

[5] V. D'Innocenzo, G. Grancini, M. J. P. Alcocer, A. R. S. Kandada, S. D. Stranks, M. M. Lee, G. Lanzani, H. J. Snaith, A. Petrozza, *Nat. Commun.* **2014**, *5*, 3586.

[6] C. Quarti, E. Mosconi, F. De Angelis, *Phys. Chem. Chem. Phys.* **2015**, *17*, 9394.

[7] J. Ma, L.-W. Wang, *Nano Lett.* **2015**, *15*, 248.

[8] D. Niesner, H. Zhu, K. Miyata, P. P. Joshi, T. J. S. Evans, B. J. Kudisch, M. T. Trinh, M. Marks, X.-Y. Zhu, *J. Am. Chem. Soc.* **2016**, *138*, 15717.

[9] W.-J. Yin, T. Shi, Y. Yan, *Appl. Phys. Lett.* **2014**, *104*, 063903.

[10] D. W. deQuilettes, S. M. Vorpahl, S. D. Stranks, H. Nagaoka, G. E. Eperon, M. E. Ziffer, H. J. Snaith, D. S. Ginger, *Science* **2015**, *348*, 683.

[11] G. Xing, N. Mathews, S. Sun, S. S. Lim, Y. M. Lam, M. Grätzel, S. Mhaisalkar, T. C. Sum, *Science* **2013**, *342*, 344.

[12] S. D. Stranks, G. E. Eperon, G. Grancini, C. Menelaou, M. J. P. Alcocer, T. Leijtens, L. M. Herz, A. Petrozza, H. J. Snaith, *Science* **2013**, *342*, 341.

[13] S. Colella, E. Mosconi, P. Fedeli, A. Listorti, F. Gazza, F. Orlandi, P. Ferro, T. Besagni, A. Rizzo, G. Calestani, G. Gigli, F. De Angelis, R. Mosca, *Chem. Mater.* **2013**, *25*, 4613.

[14] E. Edri, S. Kirmayer, A. Henning, S. Mukhopadhyay, K. Gartsman, Y. Rosenwaks, G. Hodes, D. Cahen, *Nano Lett.* **2014**, *14*, 1000.

[15] C. Wehrenfennig, G. E. Eperon, M. B. Johnston, H. J. Snaith, L. M. Herz, *Adv. Mater.* **2014**, *26*, 1584.

[16] B. Yang, J. Keum, O. S. Ovchinnikova, A. Belianinov, S. Chen, M.-H. Du, I. N. Ivanov, C. M. Rouleau, D. B. Geohegan, K. Xiao, *J. Am. Chem. Soc.* **2016**, *138*, 5028.

[17] S. T. Williams, F. Zuo, C.-C. Chueh, C.-Y. Liao, P.-W. Liang, A. K.-Y. Jen, *ACS Nano* **2014**, *8*, 10640.

[18] Y. Tidhar, E. Edri, H. Weissman, D. Zohar, G. Hodes, D. Cahen, B. Rybtchinski, S. Kirmayer, *J. Am. Chem. Soc.* **2014**, *136*, 13249.

[19] Y. Luo, S. Gamliel, S. Nijem, S. Aharon, M. Holt, B. Stripe, V. Rose, M. I. Bertoni, L. Etgar, D. P. Fenning, *Chem. Mater.* **2016**, *28*, 6536.

[20] V. L. Pool, A. Gold-Parker, M. D. McGehee, M. F. Toney, *Chem. Mater.* **2015**, *27*, 7240.

[21] G.-J. A. H. Wetzelaer, M. Scheepers, A. M. Sempere, C. Momblona, J. Ávila, H. J. Bolink, *Adv. Mater.* **2015**, *27*, 1837.

[22] B. Suarez, V. Gonzalez-Pedro, T. S. Ripolles, R. S. Sanchez, L. Otero, I. Mora-Sero, *J. Phys. Chem. Lett.* **2014**, *5*, 1628.

[23] S. Shao, M. Abdu-Aguye, T. S. Sherkar, H.-H. Fang, S. Adjokatse, G. ten Brink, B. J. Kooi, L. J. A. Koster, M. A. Loi, *Adv. Funct. Mater.* **2016**, *26*, 8094.

[24] A. M. Soufiani, F. Z. Huang, P. Reece, R. Sheng, A. Ho-Baillie, M. A. Green, *Appl. Phys. Lett.* **2015**, *107*, 231902.

[25] M. E. Ziffer, J. C. Mohammed, D. S. Ginger, *ACS Photonics* **2016**, *3*, 1060.

[26] A. J. Neukirch, W. Nie, J.-C. Blancon, K. Appavoo, H. Tsai, M. Y. Sfeir, C. Katan, L. Pedesseau, J. Even, J. J. Crochet, G. Gupta, A. D. Mohite, S. Tretiak, *Nano Lett.* **2016**, *16*, 3809.

[27] X. Zhang, G. Lu, *J. Chem. Phys.* **2015**, *143*, 064110.

[28] S. Refaely-Abramson, M. Jain, S. Sharifzadeh, J. B. Neaton, L. Kronik, *Phys. Rev. B* **2015**, *92*, 081204(R).

[29] W.-J. Yin, T. Shi, Y. Yan, *Adv. Mater.* **2014**, *26*, 4653.

[30] D. W. deQuilettes, W. Zhang, V. M. Burlakov, D. J. Graham, T. Leijtens, A. Osherov, V. Bulovi, H. J. Snaith, D. S. Ginger, S. D. Stranks, *Nat. Commun.* **2016**, *7*, 11683.

[31] J.-C. Blancon, W. Y. Nie, A. J. Neukirch, G. Gupta, S. Tretial, L. Cognet, A. D. Mohite, J. J. Crochet, *Adv. Funct. Mater.* **2016**, *26*, 4283.

[32] T. Leijtens, G. E. Eperon, A. J. Barker, G. Grancini, W. Zhang, J. M. Ball, A. R. S. Kandada, H. J. Snaith, A. Petrozza, *Energy Environ. Sci.* **2016**, *9*, 3472.

[33] J. Endres, D. A. Egger, M. Kulbak, R. A. Kerner, L. Zhao, S. H. Silver, G. Hodes, B. P. Rand, D. Cahen, L. Kronik, A. Kahn, *J. Phys. Chem. Lett.* **2016**, *7*, 2722.

[34] J. M. Frost, K. T. Butler, F. Brivio, C. H. Hendon, M. van Schilfgaarde, A. Walsh, *Nano Lett.* **2014**, *14*, 2584.

[35] J. Liu, O. V. Prezhdo, *J. Phys. Chem. Lett.* **2015**, *6*, 4463.

[36] T. S. Sherkar, C. Momblona, L. Gil-Escrig, J. Ávila, M. Sessolo, H. J. Bolink, L. Jan Anton Koster, *ACS Energy Lett.* **2017**, *2*, 1214.

[37] W. Zhang, S. Pathak, N. Sakai, T. Stergiopoulos, P. K. Nayak, N. K. Noel, A. A. Haghighirad, V. M. Burlakov, D. W. deQuilettes, A. Sadhanala, W. Li, L. Wang, D. S. Ginger, R. H. Friend, H. J. Snaith, *Nat. Commun.* **2015**, *6*, 10030.

[38] G. Sadoughi, D. E. Starr, E. Handick, S. D. Stranks, M. Gorgoi, R. G. Wilks, M. Bär, H. J. Snaith, *ACS Appl. Mater. Interfaces* **2015**, *7*, 13440.

[39] C. Qin, T. Matsushima, T. Fujihara, W. J. Potscavage Jr., C. Adachi, *Adv. Mater.* **2016**, *28*, 466.

[40] A. Baumann, S. Väth, P. Rieder, M. C. Heiber, K. Tvingstedt, V. Dyakonov, *J. Phys. Chem. Lett.* **2015**, *6*, 2350.

[41] S. Heo, G. Seo, Y. Lee, D. Lee, M. Seol, J. Lee, J.-B. Park, K. Kim, D.-J. Yun, Y. S. Kim, J. K. Shin, T. K. Ahn, M. K. Nazeeruddin, *Energy Environ. Sci.* **2017**, *10*, 1128.

[42] S. D. Stranks, V. M. Burlakov, T. Leijtens, J. M. Ball, A. Goriely, H. J. Snaith, *Phys. Rev. Appl.* **2014**, *2*, 034007.

[43] M.-H. Du, *J. Phys. Chem. Lett.* **2015**, *6*, 1461.

[44] M. J. Simpson, B. Doughty, B. Yang, K. Xiao, Y.-Z. Ma, *J. Phys. Chem. Lett.* **2015**, *6*, 3041.

[45] G. E. Eperon, D. S. Ginger, *Nat. Energy* **2016**, *1*, 16109.

[46] S. D. Stranks, P. K. Nayak, W. Zhang, T. Stergiopoulos, H. J. Snaith, *Angew. Chem., Int. Ed.* **2015**, *54*, 3240.

[47] Q. Chen, H. Zhou, Y. Fang, A. Z. Stieg, T.-B. Song, H.-H. Wang, X. Xu, Y. Liu, S. Lu, J. You, P. Sun, J. McKay, M. S. Goorsky, Y. Yang, *Nat. Commun.* **2016**, *6*, 7269.

[48] J. Chae, Q. Dong, J. Huang, A. Centrone, *Nano Lett.* **2015**, *15*, 8114.

[49] E. M. Hutter, G. E. Eperon, S. D. Stranks, T. J. Savenije, *J. Phys. Chem. Lett.* **2015**, *6*, 3082.

[50] J. M. Richter, M. Abdi-Jalebi, A. Sadhanala, M. Tabachnyk, J. P. H. Rivett, L. M. Pazos-Outón, K. C. Gödel, M. Price, F. Deschler, R. H. Friend, *Nat. Commun.* **2016**, *7*, 13941.

[51] C. Li, J. Wei, M. Sato, H. Koike, Z.-Z. Xie, Y.-Q. Li, K. Kanai, S. Kera, N. Ueno, J.-X. Tang, *ACS Appl. Mater. Interfaces* **2016**, *8*, 11526.

[52] S. D. Stranks, *ACS Energy Lett.* **2017**, *2*, 1515.

[53] L. M. Pazos-Outón, M. Szumilo, R. Lamboll, J. M. Richter, M. Crespo-Quesada, M. Abdi-Jalebi, H. J. Beeson, M. Vrućinić, M. Alsari, H. J. Snaith, B. Ehrler, R. H. Friend, F. Deschler, *Science* **2016**, *351*, 1430.

[54] E. Mosconi, D. Meggiolaro, H. J. Snaith, S. D. Stranks, F. De Angelis, *Energy Environ. Sci.* **2016**, *9*, 3180.

[55] A. Walsh, D. O. Scanlon, S. Chen, X. G. Gong, S.-H. Wei, *Angew. Chem., Int. Ed.* **2015**, *54*, 1791.

[56] J. M. Azpiroz, E. Mosconi, J. Bisquert, F. De Angelis, *Energy Environ. Sci.* **2015**, *8*, 2118.

[57] A. Swarnkar, A. R. Marshall, E. M. Sanehira, B. D. Chernomordik, D. T. Moore, J. A. Christians, T. Chakrabarti, J. M. Luther, *Science* **2016**, *354*, 92.

[58] J. F. Galisteo-López, M. Anaya, M. E. Calvo, H. Míguez, *J. Phys. Chem. Lett.* **2015**, *6*, 2200.

[59] H.-H. Fang, S. Adjokatse, H. Wei, J. Yang, G. R. Blake, J. Huang, J. Even, M. A. Loi, *Sci. Adv.* **2016**, *2*, e1600534.

[60] G. Kresse, J. Furthmuller, *Phys. Rev. B* **1996**, *54*, 11169.

[61] S. Grimme, *J. Comput. Chem.* **2006**, *27*, 1787.

[62] P. E. Blöchl, *Phys. Rev. B* **1994**, *50*, 17953.

[63] J. P. Perdew, K. Burke, M. Ernzerhof, *Phys. Rev. Lett.* **1996**, *77*, 3865.

[64] W.-J. Yin, T. Shi, Y. Yan, *J. Phys. Chem. C* **2015**, *119*, 5253.

[65] T. Shi, W.-J. Yin, Y. Yan, *J. Phys. Chem. C* **2014**, *118*, 25350.

[66] X. Zhang, Z. Li, G. Lu, *J. Phys.: Condens. Matter* **2012**, *24*, 205801.

[67] J. C. de Mello, H. F. Wittmann, R. H. Friend, *Adv. Mater.* **1997**, *9*, 230.